Phase conjugate holographic system for high resolution particle image velocimetry

Donald H. Barnhart, Ronald J. Adrian, and George C. Papen

University of Illinois at Urbana-Champaign
Urbana, Illinois 61801

ABSTRACT

A novel holographic particle image velocimeter system has been developed for the study of three-dimensional fluid velocity fields. The recording system produces three-dimensional particle images with resolution, signal-to-noise ratio, accuracy and derived velocity fields that are comparable to high-quality two-dimensional photographic PIV (particle image velocimetry). The high image resolution is accomplished by using low f-number optics, a fringe stabilized processing chemistry, and a phase conjugate play-back geometry that compensates for aberrations in the imaging system. In addition, the system employs a reference multiplexed, off-axis geometry for determining velocity directions using the cross-correlation technique, and a stereo camera geometry for determining the three velocity components. The combination of the imaging and reconstruction sub-systems make the analysis of volumetric PIV domains feasible.

Key words: Particle image velocimetry, holography, velocimetry.

1. Introduction

Photographic and videographic particle image velocimetry techniques use laser light sheets and planar imaging to measure the two in-plane components of velocity over a plane of a moving fluid medium. These methods have reached a stage of advanced development in which they are able to provide accurate measurements of the velocity field with good spatial resolution.[1] The measurements can be generalized to three-

dimensional vectors on planar domains by means of stereographic imaging[2,3] with a satisfactory accuracy in the out-of-plane component. Further generalization to three-dimensional vectors in volumetric domains is accomplished by two different approaches: photogrammetric imaging and holographic recording. The former method records several two-dimensional views with large depth-of-focus, matches the images from the different views, and tracks the motion of individual particles over two or more exposures. To perform the matching reliably, it is necessary to restrict the number of particles in the volume to maximum values that are of the order of several thousand particles.[4-6] The spatial resolution is less than that of planar PIV, fundamentally because the large depth-of-field necessitates an increase in the diffraction limited spot size of the particle images.

Measurements of certain types of fluid flows (i.e. turbulence) require good accuracy, good spatial resolution, and relatively large volumetric domains. Two essential aspects of turbulent motion are a large range of spatial scales and a large range of velocity scales. Successful measurements of turbulent flow therefore require instruments with large dynamic ranges in space and velocity, where the dynamic range is defined as the ratio of the largest measurable quantity to the smallest measurable quantity. For a given size of the measurement domain and given full-scale velocity, the dynamic ranges are maximized by minimizing the size of the smallest resolvable measurement volume and the magnitude of the noise in the velocity measurements. High quality turbulence measurements demand dynamic ranges in excess of 50-100:1 in both space and velocity.

Particle images can be recorded with good resolution in deep volumetric domains using the techniques of holography, and a number of projects to develop holographic PIV have been reported in recent years.[7-16] Many of these efforts use relatively low numbers of particles with the consequence that the spatial resolution is not much better than that of photogrammetric methods. However, holographic PIV holds the promise of being able to record large numbers of fine particles, of the order of several million, making highly resolved volumetric measurements possible. The challenges for HPIV are to record images of millions of micron-sized particles, to record over relatively large regions, and to record with near diffraction limited resolution, especially in the third dimension. The authors are not aware of this combination of performance factors being achieved in any HPIV system that has been reported to date.

This paper describes a complete holographic PIV system that has been constructed for the purpose of studying three-dimensional turbulence structure. In view of the foregoing observations, the major goals which have guided the development of the system are to make measurements with one millimeter resolution over a $100\times100\times100$ mm^3 cube with

accuracy better than one-percent of full scale, i.e. 100:1 dynamic ranges in space and velocity. To achieve these goals, the maximum displacement of the particles between laser pulses must not exceed a fraction (typically one-quarter) of the one millimeter size of a resolution cell (denoted by d_l), and for accuracy, the image diameter d_τ should be a small fraction of this displacement. This implies values for d_τ less than about 25 *microns*. The requirement for submillimeter depth-of-focus places an even greater restriction on d_τ such that image diameters less than 10 *microns* are desirable.

To measure continuous velocity fields, it is necessary to extract velocity data from nearly every resolution cell in the measurement domain, and since the particles are randomly distributed, the only way to guarantee this is to place many particles in each cell on average, e.g. the high image density PIV mode[1]. (It can be shown that interpolation over sparse sample points located randomly in space cannot retrieve motions whose wavelengths are approximately less than the mean spacing of the samples. Thus, low image density PIV is more properly restricted to studies of smooth, large scale fields.) These considerations lead to large numbers of particles ($\sim 10^7$ in a 100 *mm* cube) which in turn create speckle noise in a holographic recording that must be suppressed by using a strong reference beam, relative to the scattered light object beam. Furthermore, with the large number of particles, the size of each particle must be restricted to a few microns to avoid overloading the fluid, either on a volume basis, or on a mass basis when the fluid is gaseous.

A final consequence of the wide range of spatial scales in turbulence is that the analysis of each hologram involves vector measurements of many cells. For the numbers cited, more than one million cells must be interrogated, a prohibitively long task unless the analysis speed can be increased substantially above the current norm of a few vectors per second.

2. Holographic imaging system

The requirement for sub-millimeter depth-of-focus limits the choice of possible holographic systems that can be used for HPIV. In-line holographic systems have difficulty generating a small depth of focus and thus are limited in the spatial resolution they can achieve. In general, the depth-of-focus is $\sim d^2/\lambda$ where d is the resolution of the imaging system and λ is the wavelength of the light. For a system to produce a 1 *mm* depth of focus at $\lambda = 0.5$ *micron*, 23 *micron* resolution is required. In the present work, an off-axis system has been developed to decrease the depth of focus and improve the signal-to-noise ratio in the recorded image.

In this section, we describe the geometry of a distortion-compensated off-axis holographic optical system that is designed to provide the high spatial resolution required to achieve small depth-of-focus and hence good spatial resolution in all three measurement directions. The system is configured to record on a single film plate images at two times from two different perspectives which provide information for reconstruction of three-dimensional vector displacements.

The recording system is shown in Figure 1. Four images are independently recorded on the same plate: two pairs in each of two distinct stereo views, each view recording images at different times. This single plate system uses dual off-axis reference beams in combination with a stereo pair of low f-number optics which project two perspectives of the particles in the flow volume away from the flow. The recording light source consists of twin synchronized, injection seeded, frequency doubled Nd:YAG lasers which produce 300 mJ pulses. Injection seeding creates nearly transform limited pulses having a coherence length of >1 m. Single pulses from each laser $I_{01}(t_1)$ and $I_{02}(t_1)$ are split at the beamsplitter BS and directed through three optical paths. The beamsplitter reflections feed two reference beam paths, while the beamsplitter transmissions feed a common illumination beam path directed through the flow volume. The transmitted beams intersect after M_6 and expand after L_4, before being collimated by L_7 and used to illuminate the flow volume. The reference beams are expanded by either L_3 or L_5, collimated by either L_6, or L_8, and directed to the film plate at the angles of $\pm50^o$ with respect to the plate normal. The reference beam energy deposited on the 4×5 in^2 film plate for one exposure is approximately 2-3 mJ. The common illumination beam is prevented from reaching the film plate by a stop, while the scattered object beams are passed through the stereo camera optics and onto the film plate.

The lasers produce double pulses I_{01}, I_{02} at a repetition rate of 10 Hz with an arbitrary time offset between the pulses, and they are shuttered to permit emissions of single sets of pulses. The first pulse illuminates the flow at time t_1. Light scattered by the particles from I_{01}, is collected by two lenses L_{11} and L_{21} which define the object beams O_1 and O_2. They provide two views of the particles at time t_1 that are used subsequently to obtain the three-dimensional motion. Each object beam is deflected by a prism and refocused to form images near the single holographic plate. Both object views (through L_{11} and L_{21}) are recorded on the plate at t_1 by using reference beam R_1. The procedure is repeated identically at time t_2 except that the flow volume viewed through L_{11} and L_{21} is recorded using reference beam R_2. Again two views are recorded, resulting in a total of four images on the holographic plate. The angle between the two object beams is approximately 30°, and was chosen to reject the on-axis illumination

4

beam and permit recording of the two perspectives onto a single holographic plate. Reference angular multiplexing of the images at t_1 and t_2 on the same plate eliminates the image registration problems which occur during analysis of images recorded on separate plates. Furthermore, it permits the use of the cross-correlation method discussed in Section 4 to find the image displacement between exposures and hence the determination of the displacement direction.

3. Distortion compensation

In order to measure velocity vectors accurate to 1%, it is necessary to minimize all sources of image distortion. There are two dominant sources of distortion in the present system. The first is the non-ideal reconstruction of the image volume resulting from aberrations in the imaging optics. As will be shown below, this effect can be compensated by using phase conjugate reconstruction. The second is the distortion resulting from physical changes in the holographic film emulsion after recording and processing. It can be minimized through the judicious choice of processing chemistry and recording geometry, as will be shown in the following section.

Phase conjugate reconstruction

The large imaging volumes used in HPIV systems result in a large range of recorded angular frequencies and require large aperture, low f-number imaging optics (f-3 for this system). In theory, the small f-numbers of the lenses used in the imaging system should produce excellent resolution and low aberration. In practice, low f-number diffraction limited optics are prohibitively expensive. However, simpler, more cost-effective optical components typically cause severe aberrations. Without some form of compensation, these aberrations significantly increase the effective f-number of the system, decrease the quality of the reconstructed images and increase the depth-of-focus to the point where it is larger than the desired resolution cell size.

The imaging aberrations are corrected by using phase conjugate reference beams during the holographic reconstruction process. In the present system, the entire imaging subsystem behind the interrogation volume in Figure 1, comprised of the four lenses (L_{11}, L_{12}, L_{21} and L_{22}), two prisms (P_1 and P_2) and film plate holder, is on a removable optical breadboard that is transferred to a separate interrogation table for reconstruction (See Figure 2). The conjugate reference beams are generated with a smaller laser, at 532 *nm*, operating in cw mode (diode pumped frequency doubled Nd:YAG). This wavelength must be the same as the recording wavelength to prevent magnification effects.

To compensate for optical aberrations, the reconstruction reference beam is the phase conjugate of the original reference beam. When the phase conjugate image propagates back through the original imaging system, the original phase front is recovered and the aberration is removed, preserving the inherent resolution of the imaging system and forming a real image that can be interrogated by a CCD camera. This phase conjugate reconstruction process is shown in Figure 2. In order for phase conjugate reconstruction to be successful, the reconstructing field R* needs to be the *exact* phase conjugate of the original reference beam. Practically, the easiest way to insure this is to have a planar reference field. The phase conjugate of such a wave-front is simply another plane wave traveling in the opposite direction. Thus, the collimation process of the original reference beams and the reconstruction reference beam is crucial for accurate aberration compensation. Also shown in Figure 2 are the two images formed by the stereo reconstruction of a single particle. While the individual images are elongated ellipsoids (measuring hundreds of *microns*), measurement of the out-of-plane particle position can be determined from the intersection of the two images which is a small fraction of the single image depth-of-focus (on the order of 10 *microns*).

Film effects

Holographic imaging results from an interferometric recording process between an object field and a reference field. During the holographic recording step, an interference pattern is formed by the two fields, having a fringe spacing on the order of *microns*. This interference pattern photochemically develops into a permanent, three-dimensional grating structure within the film emulsion. During reconstruction, the object field is reproduced by diffracting a second reference field off this recorded grating structure. Unfortunately, the chemical processing of the film typically produces a distorted grating structure, resulting in a distorted reconstructed object field. The distortion is minimized by a judicious choice of the chemistry used in film processing and the geometry used in recording. It will be shown that for large recorded image volumes and wide ranges of recorded angular frequencies, an off-axis transmission geometry produces the least distortion.

For the holographic film used in this system, grating distortion is caused by the shrinkage of the gelatin suspension that contains the silver halide grains, and is caused by material removal during the development process. This change in emulsion volume results in a corresponding change in the recorded fringe pattern.[17] It should be noted that while distortionless, dry-process holographic media do exist (ie photopolymers,

thermoplastics), the forms presently available have setbacks (ie low light sensitivity, reference selection ambiguity) preventing their use in this application.

A simple model for emulsion shrinkage can be developed by applying wave vector analysis to the recording geometry (see Figure 3). Because of the open boundary on the emulsion surface, volumetric changes occur principally in the direction normal to the film surface. This anisotropic shrinkage results in a directional skewing of the recorded grating vector $\mathbf{K}$; where $\mathbf{K}$ is defined by the difference of the reference wave vector $\bar{\mathbf{k}}_r$ and the object wave vector $\bar{\mathbf{k}}_o$ inside the film emulsion:

$$\mathbf{K} = \bar{\mathbf{k}}_o - \bar{\mathbf{k}}_r \tag{1}$$

where the overbars denote the wave vectors inside the emulsion.

Shrinkage in $\mathbf{K}$ results in a distorted grating vector $\mathbf{K_d}$, which is quantified by decomposing the grating vector $\mathbf{K}$ into orthogonal components lying parallel ($\mathbf{K_\parallel}$) and perpendicular ($\mathbf{K_\perp}$) to the emulsion surface, and then rescaling $\mathbf{K_\perp}$ by the emulsion shrinkage factor S:

$$\mathbf{K_d} = \mathbf{K_\parallel} + \frac{1}{1-S}\mathbf{K_\perp} \tag{2}$$

where S represents the fractional amount of shrinkage in the normal direction.

The ratio of $\mathbf{K_\parallel}$ to $\mathbf{K_\perp}$ depends on the recording geometry, and in the following analysis, three geometries are considered: in-line, off-axis transmission, and off-axis reflection. The in-line geometry (Figure 3c) has its reference direction normal to the film plate surface ($\theta_r = 90°$), while the off-axis transmission geometry (Figure 3d) has its reference beam angle at $\theta_r = 40°$ from the plate surface on the same side of the incident object wave-front. The off-axis reflection geometry (Figure 3e) has its reference direction vector positioned at $\theta_r = -40°$ from plate surface, impinging onto the opposite side of the surface as the incident object wave-front. Note that the standard convention of defining object and reference angles with respect to the surface normal is not followed here. Instead, by defining the angles with respect to the film surface, the reflection hologram geometry has negative angles ($-180° < \theta_r < 0°$) while the transmission geometry has only positive angles ($0° < \theta_r < 180°$). In addition, the object angles will always take on positive values ($0° < \theta_o < 180°$). From Figure 3, it is clear that the in-line geometry has the smallest $\mathbf{K_\perp}$ component, while the reflection geometry has the largest. Thus, for object

wave vectors near the surface normal ($\theta_0 \sim 90°$) film shrinkage causes the smallest distortion in the in-line geometry.

Refraction at the air/emulsion interface also effects distortion and the effects are different for the recording and playback process. During holographic recording, the air/emulsion interface creates angular shifts in the interference fringes formed within the emulsion. For reflection holograms, where k_0 and k_r are incident from opposite sides of the plate, K is bent toward the surface normal, resulting in a larger $K_\perp$ and thus more distortion, as can be seen in Eq.(2). In the limiting case where both $k_0 = -k_r$ on the normal, K is equal to $K_\perp$. For transmission holograms, where k_0 and k_r are incident from the same side of the plate, K is tilted away from the surface normal, resulting in a smaller $K_\perp$ and less distortion. In the limiting case where k_0 and k_r are symmetric about the normal, no distortion occurs.

During image reconstruction, additional distortion occurs. Because of the emulsion shrinkage, the reconstructed object wave vector inside the film emulsion $\overline{k}_{od}$ is tilted relative to the original object wave vector $\overline{k}_o$. Outside the film emulsion, the tilt of k_{od} is compounded by the $\cos\theta$ dependence of refraction at the emulsion/air interface.

The distortion in the reconstructed object field may be quantified in several ways. The absolute angular distortion θ_s is defined as the angular deviation of reconstructed object wave vector k_{od} from the original object wave vector k_o due to the tilt in the grating wave vector. (see Figure 3a). The absolute image displacement at some distance from the plate is $\theta_s d_s$, where d_s is the effective distance from the film plate to the image volume when no focusing optics are present.

The following results are based on uniform emulsion shrinkage and include the refractive effects of the emulsion/air interface. Shrinkage values are based on measurements reported for various process chemistries.[17] Figure 4a is a contour plot of the calculated absolute image displacement $\theta_s d_s$ for an effective distance of $d_s = 250\ mm$ as a function of the object and reference beam angles (θ_0, θ_r) using a shrinkage value of $S = 0.5\%$. The object angular frequencies are plotted over a range of 55° - 125° with respect to the film surface, with $\theta_0 = 90°$ being normal incidence, and reference angles θ_r ranging between 40° and 90°. This range corresponds to the f-number of the holographic system with the left channel of the system covering $\theta_0 = 55° - 95°$, and the right channel of system having a range between $\theta_0 = 85°$ and $\theta_0 = 125°$. As expected, the in-line geometry ($\theta_r = 90°$) has the least absolute image displacement for object angles near normal incidence ($\theta_0 \sim 90°$). However, we will show below that the off-axis transmission geometry ($\theta_r = 40°$) yields the least absolute image displacement across the entire range of object angles used by the holographic imaging system.

Figures 4b-4d show the relative effects of the processing chemistry and recording geometry on the absolute image displacement $\theta_s d_s$. The three emulsion shrinkages shown have been chosen as representative of typical process chemistries.[17] Figure 4b shows that for a 15% emulsion shrinkage, unacceptable shifts result which range between -2.5 mm and 2.5 mm. The in-line technique is again superior to the other geometries for object angles near normal incidence ($80°<\theta_O<100°$). However, for object angles outside this range, it also has significant distortion. The reflection geometry, owing to the grating vector being nearly perpendicular, is inferior to both in-line and off-axis geometries. Figure 4c shows the current process chemistry in use, having a 0.5% shrinkage.[17] The distortion, although still significant, is greatly diminished from Figure 4b. This result emphasizes the importance of the development chemistry on the performance of the overall system. Figure 4d shows the performance when the emulsion shrinkage is 0.1%. This value was chosen to represent potential process improvements beyond the chemical processing in current use.

The phase conjugate reconstructed particle image size is dependent on the total range ($k_{od_{max}}$ to $k_{od_{min}}$) of wave vectors that scatter from the object and intercept the film plate. A measure of the formed particle image size at an imaging distance d_s is given by the displacement range $d_s (\theta_{max}-\theta_{min})|_{window}$, where θ_{max} and θ_{min} are the angles associated with $k_{od_{max}}$ and $k_{od_{min}}$ and window refers to the aperturing effect of the system that limits the angles that intercept the film plate. With no distortion, $\theta_{max}=\theta_{min}$ for any window, and, for small particles, the particle image size is limited by diffraction through the system. With distortion, for small particles and low f-numbers, the particle image size is limited by the geometric point-spread function, being larger than indicated for diffraction alone.

Each of the stereo imaging channels pass a distinct range of angular frequencies. The center angles of these windows are symmetric about the film surface normal (see Figures 1 and 2.) The two image configuration used implies that image sizes must be minimized over a wide range of window center frequencies that lie away from the film plate normal. In contrast, traditional on-axis single channel imaging systems require optimal imaging performance over a smaller range of center frequencies which lie close to the film plate normal.

Figure 5 plots displacement range $d_s (\theta_{max}-\theta_{min})|_{window}$ as functions of window center angle, θ_O, and reference angle, θ_r, for $d_s = 250$ mm, where the window size = 10°. Figure 5a is a contour plot of the displacement range as a function of the window center angle, θ_O, and reference angles, θ_r, using a shrinkage value of 0.5%. Although the in-line geometry is still superior for angles near normal incidence, the off-axis transmission

geometry results in smaller displacement ranges over the *full* range of window center angles used between both stereo channels. Figure 5b (S = 15%) shows a maximum displacement range of 1500 *microns* for the off-axis case, 2000 *microns* for the in-line case, and >10,000 *microns* for reflection geometry. Figure 5c (S = 0.5%) shows a maximum displacement range of 32 *microns* for the off-axis case, 55 *microns* for the in-line case, and ~400 *microns* for reflection geometry. Finally, Figure 5d showing the least distorted case (S = 0.1%), with the maximum displacement range of 6 *microns* for the off-axis case and 12 *microns* for the in-line case, and ~80 *microns* for reflection geometry. By examining Figure 4a and 5a it can be seen that the optimal angle for minimum image size is not at 40°, but is actually closer to 60°. The 40° reference beam angle was therefore chosen for physical layout reasons and not because it was optimal.

An additional image distortion effect, identified during the development of this system, results from nonuniform spatial variations in emulsion shrinkage and reference beam phase. It was determined that the scattered light from each particle must subtend a region not greater than ~1 cm^2, when projected at the holographic plate, in order to produce good images. These distortions are not generally observed with in-line techniques because the dominant energy in the forward direction within the dynamic range of the film is already contained within a small solid angle about the illumination axis and thus produces small projected images at the film plate. The side scatter used in the off-axis technique is more uniformly distributed in angle, and thus for the same dynamic range of the film, records a larger angular distribution of scattering, which in turn produces the improvement in the depth of field. However, this larger range of recorded scattered angles may not generate an equivalent improvement in the reconstructed image if non-uniform shrinkage and reference phase variations are present over the total range of scattered angles that are recorded. To minimize these effects, the projected image size is kept to a minimum either by locating the film plate close to the particle space or by imaging the particles close to the film plate. The phase variations in the reference field are also minimized by using a well collimated reference field. For large image volumes and small particle sizes, it is extremely difficult to produce a projected area of ~1 cm^2 without using lenses and in order to produce a sub-millimeter depth of focus, these lenses must have low *f*-numbers. Thus, to minimize spatially non-uniform distortion effects in the film, lenses are used to project the recorded volume near the film plate, and to compensate for the distortion from this imaging, the phase conjugate reconstruction geometry is used. It is the combination of both of these techniques which produces high quality particle images.

Incorporating the distortion model into an optical ray-tracing program, along with the actual lens and prism characteristics, the effect of the fringe distortion on the size of the actual reconstructed image can be assessed. This has been done using a ray-tracing program.[18] A point source of rays was located at the center of the particle space and the marginal and center rays were propagated through the camera optics to the hologram surface. The rays were then modified by scaling $K_\perp$ and propagated from the hologram back through the same camera optics. The size of the locus of rays intersecting a plane positioned at the center of the particle space yielded the geometrical point spread function of the system. For a shrinkage factor of 0.5%, the in-line geometry produced a 90 *micron* image, the transmission geometry produced a 40 *micron* image, and the reflection geometry produced a 550 *micron* image. For a shrinkage value of 0.1%, the off-axis transmission geometry was found to have an 8 *micron* image size. These values are consistent with experimental values obtained using phase conjugate reconstruction as will be shown below.

Experimentally measured particle image sizes of 0.5-1 *micron* diameter oil droplets are shown in Figures 6 and 7. Figure 6 shows the horizontal and vertical intensity particle image cross-sections within the holographic reconstruction, measured by placing a bare CCD array at the image focus. The reconstructed particle images were approximately 30 *microns* in the horizontal and 15 *microns* in the vertical directions. The larger horizontal size is consistent with the film distortion analysis, owing to the horizontal grating vector. The three-dimensional particle image intensity distributions shown in Figure 7 were obtained by phase conjugate reconstruction of the image volume through a single imaging channel and digitally sampling a stack of twenty planes using a bare CCD array. The sampled planes were spaced 50 *microns* apart, within a 1 mm^3 reconstruction cell taken from within a larger imaged volume of 15.5×16.5×33.0 mm^3. The resulting image was thresholded slightly above the background noise level (as seen in Figure 6). Each particle image stack forms a three-dimensional ellipsoid with its long dimension providing a measure of depth-of-focus and oriented parallel to the optical axis. As can be seen clearly in the figure, the depth of focus varies between 100 and 700 *microns*, depending on the particle size (averaging 0.5-1 *micron*). In contrast, previously conducted simple in-line experiments revealed a much larger depth-of-focus which varied between 1.5 *mm* and 6 *cm*, depending on the particle size (1 *micron* - 50 *microns*) and the scattered object to unscattered reference beam ratio. In addition, Figures 6(a) and (b) show that the signal-to-noise ratio obtained with a relatively large number of particles was excellent. Without phase-conjugation, the imaging system failed to produce *any*

recognizable images. Hence, phase-conjugate reconstruction is an essential element in this design.

4. Interrogation system

In outline, the interrogation involves three steps: measurement of the two-dimensional displacements of the images recorded and reconstructed though L_{11}-P_1-L_{12}; measurement of the two-dimensional displacements of the images recorded and reconstructed though L_{21}-P_2-L_{22}; and computation of the three-dimensional displacements from the two sets of two-dimensional measurements. As such, the procedure is quite similar to stereo PIV with photographic recording[3], but we shall see that there are several important differences.

To reconstruct and interrogate the individual volumetric interrogation cells, the entire imaging sub-assembly (L_{11}, P_1, L_{12}, L_{21}, P_2, L_{22}, plus the developed film plate, as shown in Figures 1, 2) is placed on a reconstruction table and two phase conjugate reference beams R_1^* and R_2^* are alternately switched to reconstruct the particle images at t_1 or at t_2. During the first interrogation, the optical path through L_{11}, P_1, L_{12} is blocked so that only the view of the particles recorded through L_{21}, P_2, L_{22} is reconstructed (See Figure 2). The images at t_1 and t_2 are reconstructed, digitized, and analyzed to determine the two-dimensional displacement field of the images as viewed through L_{21}. This procedure is applied to the entire reconstructed volume by scanning the digitizing camera over many XY planes. Next, the optical path through L_{21}, P_2, L_{22} is blocked so that only the view of the particles recorded through L_{11}, P_1, L_{12} is reconstructed. The procedure described above is repeated to obtain the two-dimensional field of particle displacements as seen through L_{21}. We refer to the procedure just described as *stereo-stereo holography* because it involves recording the images stereoscopically and reconstructing them stereoscopically. It is not the same as reconstructing a single holographic image and viewing it stereoscopically.

It is important to note that the holographic plate records *four images of each particle*, one from each viewing direction at each time. The two viewing directions for recording make it possible to reconstruct the images with good intensity in two widely separated directions. For example, the scattering particles employed in the present experiments are *0.5-1 micron* oil droplets in air, and these are very weak scatterers, much smaller than the *30-40 micron* particles used in HPIV experiments that have been reported earlier. Perhaps more importantly, the two viewing directions also make it possible to reconstruct each view separately.

Images are digitized by placing a 1035×1320 pixel CCD array (Videk Megaplus *sans lens*) in an X-Y plane in the space of the reconstructed image. The CCD array, mounted on a computer controlled XYZ table, covers only a small part of a complete X-Y plane. It senses a cross-section of each particle image, the cross-section being slightly larger than the diameter of the image since particle images intersect the plane of CCD array at a relatively small angle (See Figure 8). The video array records the image field at time t_1 reconstructed by phase conjugate reference beam R_1^*, and transfers it to a computer. Then it records the image at t_2 reconstructed by R_2^*, and passes it to the computer as a second, separate buffer. While the video array is moved to the next location in the X-Y plane, the computer determines the two-dimensional displacements dX between the two exposures by procedures that have been developed previously for the analysis of two-dimensional photographic PIV data. Specifically, the image array is sub-divided into interrogation spots that contain many (~10) particle images, and the displacement of the *group of images* in each spot is found by cross-correlating the images of the first and second exposures.[19,20]

There are several important consequences of using image correlation analysis to find displacements.[19] Correlation does not require image matching on a particle-by-particle basis, nor does it attempt to track particles in three dimensions. Provided that the concentration of particles is high enough, each interrogation cell yields a displacement vector measurement, and the vectors can be evaluated on a uniform, non-random grid. The two-dimensional procedure used in the present work is built on planar scanning technology that is well established for the analysis of photographic PIV images.

Relative to auto-correlation analysis of PIV images, cross-correlation permits small displacements (hence, larger velocity dynamic range), and it determines the direction of the displacements and improves the signal-to-noise ratio. These advantages come at the cost of transferring twice as much image data and performing three FFT computations instead of two for autocorrelation.

The hardware and software system used to analyze HPIV data should be much faster than that of a typical planar PIV in order to process conveniently the large amount of data generated by the extension to volumetric vector fields. For example, with the present approach, the analysis of one 100×100×100 mm^3 volume with 1 mm resolution requires 2×10^6 measurements of vector displacement, the same number as the analysis of two-hundred 100 mm ×100 mm photographs. To meet this demand a parallel processor computer system was constructed using eight i860-based attached processors (*Mercury Computer MC860VS*) in a *Sun 4/370* host[20]. Its aggregate peak processing speed is 640 *Mflop*. It uses completely digital cross-correlation analysis with an adaptive windowing

method to enhance signal recovery. Using pipe-lined processing and careful load balancing it has been possible to achieve single-frame cross-correlation speeds in excess of 100 vectors per second based on 128×128 pixel interrogation domains. The peak theoretical auto-correlation speed is 160 vectors per second, based on the FFT computation time for the *MC860VS*, but with overheads(data transfers, peak searches, etc.) the achievable rate is lower. (For comparison, the peak rate for Young's fringe analysis is calculated to be 266 vectors per second, including overheads.)

At any given location of the CCD array within the t_1 reconstruction the input image is digitized onto a 1024 ×1024 array which is subdivided into eight 512× 256 (nominal) processor arrays that are passed to each of the eight attached processors. The reference beam is switched to reconstruct the image at t_2 , and this data is stored in the array processor memories in a fashion similar to the t_1 data. Within each processor the processor arrays are further divided into correlation blocks which each contain two data windows. Window 1 contains I_1 ,the image intensity from the exposure at t_1, and Window 2 contains I_2 , the image intensity field from the exposure at t_2. These windows are cross-correlated according to

$$C(\mathbf{s}) = \int I_1(\mathbf{X}) I_2(\mathbf{X} - \mathbf{s}) d\mathbf{X} \qquad (3)$$

The size of Window 1 is adapted to the flow field to give the smallest area (maximum resolution) that contains enough images to produce reliable interrogation. The size and offset of Window 2 are determined by the character of the velocity field. They may be set according to *a priori* knowledge, and the offset can be set dynamically during the interrogation. If there is no knowledge available about the flow, the windows are not offset, but the second window can be made larger than the first window so as to maximize the number of particles images in the second window that were also in the first window. If the second window is made large enough, the loss of pairs is determined solely by the out-of-plane displacements. Further details are given in Reference 20.

The effective thickness of an interrogation cell is the depth of focus of the reconstructed images, and the volume of an interrogation cell is the intersection of the first window with this thickness. Typically, the interrogation cells are located on grid of points that are spaced so as to overlap the cells by 50%. This rate of sampling in the spatial domain approximately satisfies the Nyquist criterion.

The relationship between two-dimensional displacements of images of a particle in the plane of the video array and the three-dimensional displacement of the particle is needed to solve for the velocity vector. As shown in Figures 7&8, the three-dimensional

particle images formed by the phase conjugate reconstruction are long, small diameter, roughly ellipsoidal volumes. The orientation of the long axis will be denoted by the unit vector q (See Figure 8). From observation, the direction of q is parallel to the axis of the focused light cone which forms the image, and to a good approximation this coincides with the chief ray of the image traced through the optics to the particle location. Thus, q varies with the location of the particle image in a predictable way. The focal spot diameter is perpendicular to the direction of q.

The images recorded at t_1 and t_2 have slightly different directions q_1 and q_2. Between exposures, the particle is displaced in the fluid by an amount $dx = u\, dt$ with dx being the corresponding displacement of the center of the holographic image. Since the length of the particle image and its displacement are each very small fractions of the distance to the optical center of the lenses L_{12} and L_{22}, the directional difference between q_1 and q_2 is normally negligible. Specifically, the fractional error incurred in evaluating dx by assuming $q_1 = q_2 = q$ is less than the ratio of the length of the image to the distance to the optical center (See Figure 8), a fraction of a per cent in most cases. Thus to a very good approximation q can taken to be constant between exposures.

Assuming that q is essentially constant, the 2-D displacement $dX=(dX,dY)$ is independent of the distances of the images from the video array plane, and the relationships between displacement and velocity are

$$dX = u\,dt - w\,dt\, q_x/q_z \qquad\qquad (4a)$$

$$dY = v\,dt - w\,dt\, q_y/q_z \qquad\qquad (4b)$$

where $u = (u,v,w)$ and $q=(q_x,q_y,q_z)$. Note that the magnification is always unity for phase-conjugated imaged reconstructions. These equations, coupled with measurements of dX from the two stereo views and a knowledge of q, provide four equations for the three components of u. The extra equation can be used to check the validity of the measurements. While it is a satisfactory approximation to treat q as a constant within a single interrogation cell, the variation of q over the entire field of view should be accounted for, either by a calibration and table look-up, or by a model of $q(x, y, z)$.

5. Vector field measurements

The present HPIV system has been used to measure air flows in a turbulent pipe having a mean velocity of 0.8 m/s and a Reynolds number on the order of 6000, where the pipe length is 10 m and pipe diameter is 76.2 mm. The air was seeded with 0.5 - 1

micron oil droplets in a concentration of ~10 droplets per mm^3. Two openings were created on opposite sides of the pipe at the location of the measurement volume to permit illumination of the test volume without excessive flare from walls. The hologram was exposed to two (10 *ns*) laser pulses with $\Delta t = 0.2$ *ms* between the pulses.

Figure 9 shows the three-dimensional velocity field obtained from the pipe flow experiment with the mean velocity subtracted. The measurement volume is $24.5 \times 24.5 \times 60$ mm^3. For clarity, only the data on the surfaces of the rectangular volume are shown. The spacing of the 50% overlapping interrogation spots is 0.435 *mm*, and the measured volume was sampled at 448,362 points. The derived three-dimensional field was obtained by imaging through the left and right camera channels separately, and twice sampling a shared-coordinate stack of 138 two-dimensional image planes. The stereo-sampled, cross-correlated displacement data was then used for composing the three-dimensional vector map. The average recovered vector success rate, after combining the results from the two channels, was better than 85 percent. By interpolating missing data, the displayed vector field fills more than 95 percent of the original sampled points. The data was low-pass filtered to remove high-frequency noise, using a three-dimensional Gaussian smoothing function with a kernel size of 1.5 grid-points in each dimension.

6. Summary

A holographic particle image velocimeter has been developed for the study of three-dimensional fluid velocity fields. A key element of this system is a unique low *f*-number optical arrangement for recording two views of the flow volume at two times on a single holographic plate, and reconstructing those views one-at-a-time using phase conjugate multiplexed image reconstruction.

Relative to in-line holographic techniques, the present system yields images with substantially smaller depth-of-focus and improved signal-to-noise ratio. Relative to conventional off-axis techniques the advantages are improved image resolution and depth-of-focus. Recording on a single plate eliminates the problem of accurately registering separately recorded images, and multiplexing the images at two times eliminates directional ambiguity in the velocity measurements and makes it possible to use cross-correlation analysis of the images, which is a preferred form of signal analysis. The optical system has been shown to image over 10^6 particles with a 20 *micron* in-plane resolution and a single channel depth-of-focus less than *1 mm*. More than 400,000 3-D velocity vectors have been extracted from a $24.5 \times 24.5 \times 60$ mm^3 measurement volume. By combining 2-D displacements from two imaging channels, the measurement accuracy

of the derived out-of-plane displacement is comparable with that of the in-plane displacement. These values are at least as good as those achieved with photographic imaging. Using 300 *mJ, 532 nm* Nd:Yag pulses, images of 0.5 - 1 *micron* particles in air can be recorded with good signal-to-noise ratio at scattering angles more than 15° away from the forward direction. Such particles are able to follow turbulent fluctuations accurately in many gaseous turbulent flows.

The optical system uses a stereo holographic recording technique in which two images are recorded from two different viewing directions, and each view is reconstructed separately. The analysis of this form of image is done without three-dimensionally tracking individual particles, thereby greatly simplifying the procedure. In the present system, the two-dimensional cross-correlation algorithms, having been used in analyzing two-dimensional displacements in PIV photographs, are used to analyze displacements in planar slices of the holographically reconstructed three-dimensional flow volume. Analysis of each stereo view permits measurement of the full three-dimensional flow vector. Implementation of this algorithm on a parallel processor makes analysis of many holograms feasible.

Acknowledgments

References

1. R. J. Adrian, "Particle-Imaging Techniques For Experimental Fluid Mechanics," Annu. Rev. Fluid Mech. **23**, 261-304 (1991).

2. M. P. Arroyo and C. A. Greated, "Stereoscopic Particle Image Velocimetry," Meas. Sci. and Tech. **2**, 1181-1186 (1991).

3. A. K. Prasad and R. J. Adrian, "Stereoscopic Particle Image Velocimetry Applied to Liquid Flows," Exper. in Fluids **15**, 49-60 (1993).

4. J. C. Kent and A. R. Eaton "Stereo Photography of Neutral Density He-Filled Bubbles for 3-D Fluid Motion in an Engine Cylinder," Appl. Optics **21**, 904-912 (1982).

5. K. Nishino, N. Kasagi, and M. Hirata, "Three-Dimensional Particle Tracking Velocimetry Based on Automated Digital Image Processing," ASME J. Fluids Engr. **111**, 384-391 (1989).

6. D. Papantoniou and H.-G. Maas "Recent Advances in 3-D Particle Tracking Velocimetry," in *Proc. 5th Intl. Symp. on Appl. of Laser Tech. to Fluid Mech.*, Lisbon, July, 1990. (Instituto Superior Tecnico: Lisbon)

7. H. Royer, "Holographic Velocimetry of Submicron Particles," Opt. Commun. **20**, 84-86 (1977).

8. W. Lauterborn and A. Vogel, "Modern Optical Techniques in Fluid Mechanics," Annu. Rev. Fluid Mech. **16**, 223-244 (1984).

9. P. H. Malyak and B. J. Thompson, "Particle Displacement and Velocity Measurement Using Holography," Opt. Engr. **23**, 567-576 (1984).

10. K. Hinsch, H. Hinrichs, G. Kufahl, and P. Meinlschmidt, "Holography with Controlled Coherence for 3-D Particle Image Velocimetry (PIV)," in Holographics 1990, (ed. T. Tschudi, Mesago Publ. Co., Nurnberg 1990), pp. 51-57.

11. M. Stanislas, M. Dadi., O. Rodriguez and A. Dyment, "A Study by Holographic Velocimetry of the Behavior of Free Small Particles in a Flow," Exp. in Fluids **10**, 285-294 (1991).

12. L. M. Weinstein, G. B. Beeler, and A. M. Lindemann, "High-Speed Holocinematographic Velocimeter for Studying Turbulent Flow Control Physics," AIAA Paper No. 85-0526, 1-9 (1985).

13. J. A. Liburdy, "Holocinematographic Velocimetry: Resolution Limitation for Flow Measurement," Appl. Opt. **26**, 4250-4255 (1987).

14. J. M. Coupland. and N. A. Halliwell, "Particle Image Velocimetry: Three-Dimensional Fluid Velocity Measurements Using Holographic Recording and Optical Correlation," Appl. Opt. **31**, 1005-1007 (1992).

15. H. Meng and F. Hussain, "Holographic Particle Velocimetry: A 3D Measurement Technique for Vortex Interactions, Coherent Structures, and Turbulence," Fluid Dyn. Res. **8**, 33-52 (1991).

16. C. S. Moraitas, *Optical Processing of Holographic Particle Records*, Ph.D. Thesis, Tech. Univ. Denmark(1992).

17. C. Kocher, *A Study of the Effects of Processing Chemistry of the Holographic Image Space* , PhD. Thesis, The British Library (1988). (Experiments for this paper used Agfa 8E56HD plates processed with Agfa-Gevaert GP62 developer followed with a rehalogenating bleach. The 15% shrinkage value is representative of fixed or solvent-bleached processes.)

18. Y. A. Carts, "Mathematica supports electro-optics users," Laser Focus World **29**, 107-108 (1993).

19. R. D. Keane and R. J. Adrian, "Theory of Cross-Correlation Analysis of PIV Images," Appl. Sci. Res. **49**, 191-215 (1992).

20. C. D. Meinhart, A. K. Prasad, and R. J. Adrian, "A Parallel Digital Processor System for Particle Image Velocimetry," Meas. Sci. and Tech., **4**, 619-626 (1993).
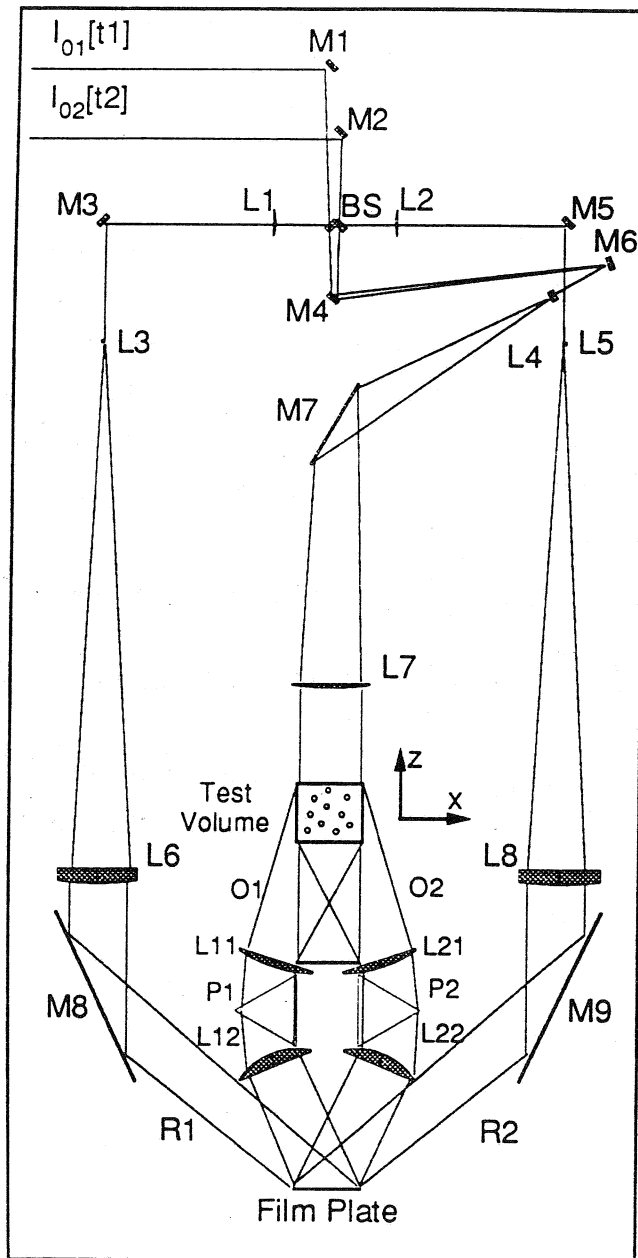
Figure 1

Optical system used in recording the hologram. Light pulses $I_{o1}[t_1]$ and $I_{o2}[t_2]$ are generated by a dual pulsed Nd:YAG laser system. A V-shaped beamsplitter is used to combine the two pulses into a common illumination path (BS, M_4, M_6, L_4, M_7, L_7), as well as to produce separated reference beams ($R_2 = BS$, L_2, M_5, L_5, L_8, M_9 and $R_1 = BS$, L_1, M_3, L_3, L_6, M_8).
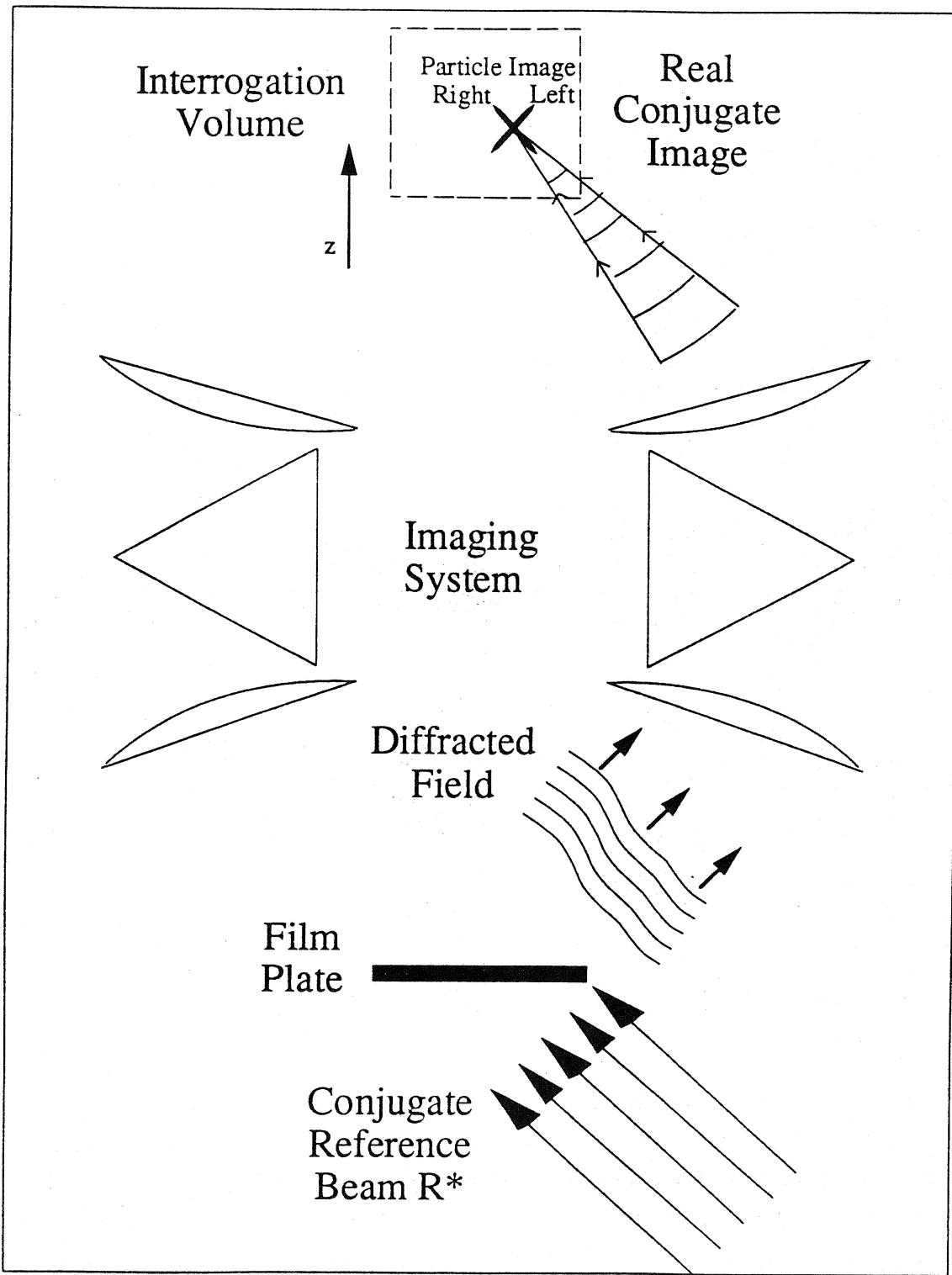
Figure 2

Imaging subsystem used for phase conjugate reconstruction. One perspective channel is shown being reconstructed. The stereo produced images of a single particle are shown in the interrogation volume as crossed ellipsoids.
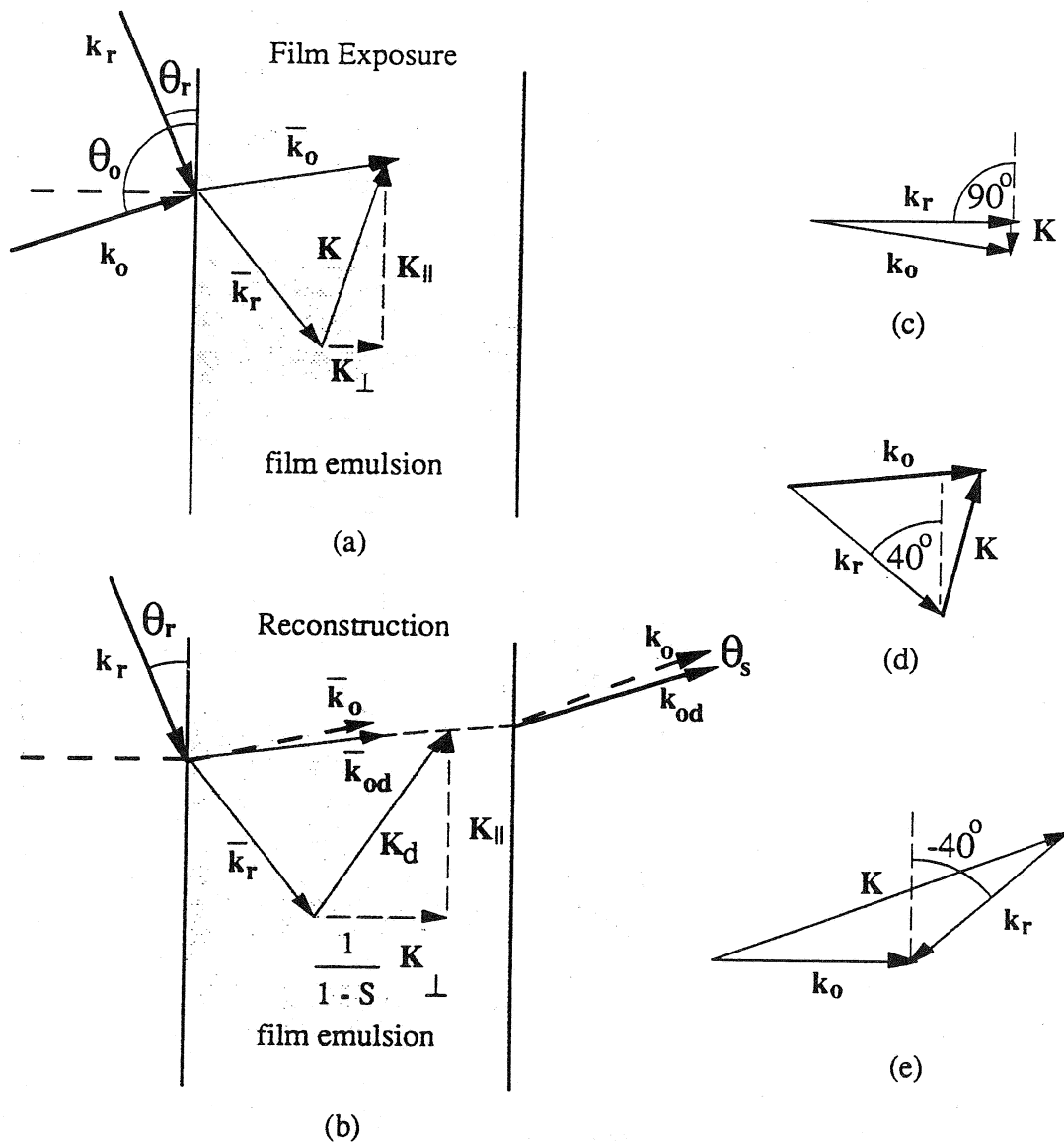
Figure 3

Grating wave vectors within the film emulsion. a) During film exposure, the refracted reference beam $\overline{k}_r$ and refracted object beam $\overline{k}_o$ produce a grating wave vector K within the emulsion with perpendicular component $K_\perp$ and parallel component $K_\parallel$. b) After development, the tilt of K_d produces an angular distortion θ_s between the reconstructed object wave vector k_{od} and the original object wave vector k_o. c) In-line recording geometry ($\theta_r = 90°$). d) Off-axis transmission geometry ($\theta_r = 40°$). e) Reflection geometry ($\theta_r = -40°$).
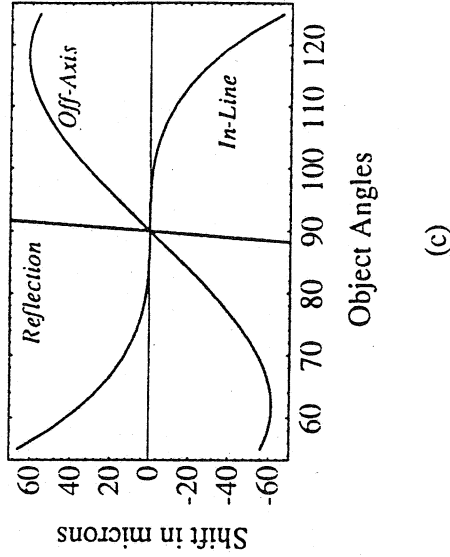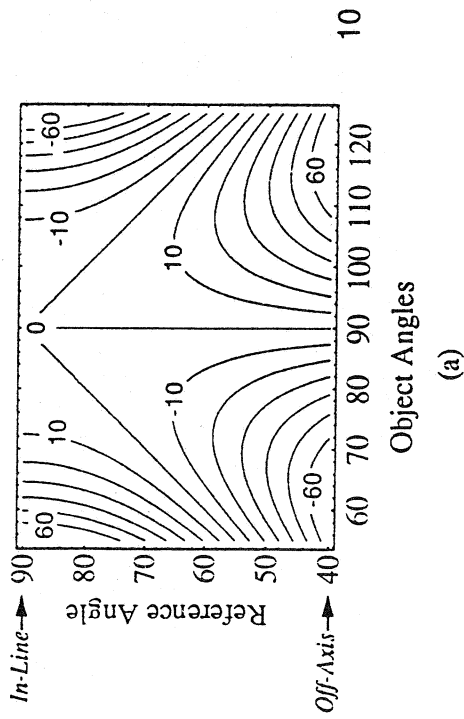
(a)

(b)

(c)

(d)

10
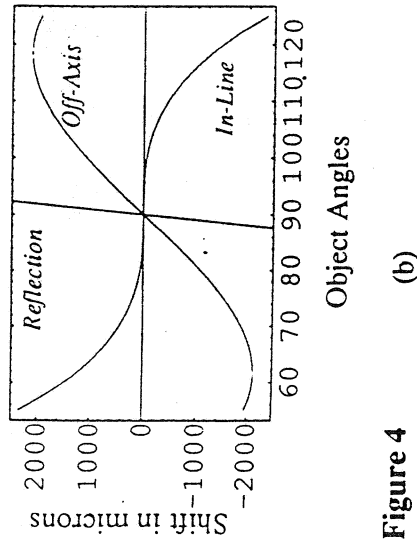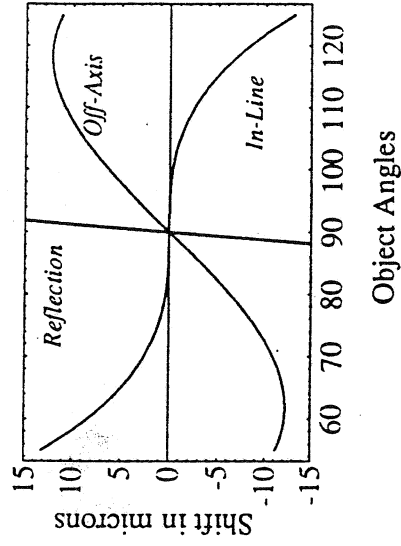
Figure 4

Film distortion effects on absolute image displacement. a) Contour plot of the absolute image displacement θ_s, d_s as a function of object and reference beam angle for a 0.5% emulsion shrinkage S and an effective distance $d_s = 250$ *mm*. Contours have 10 *micron* intervals. Two of the recording geometries are labeled on the y-axis. The reflection geometry ($\theta_r = -40°$) is not shown. b)-d) Slices of the contour plot for fixed reference beam angles ($\theta_r = 90°$, $40°$, $-40°$) corresponding to each geometry (in-line, off-axis, reflection) for different values of S. b) 15% c) 0.5% d) 0.1%.
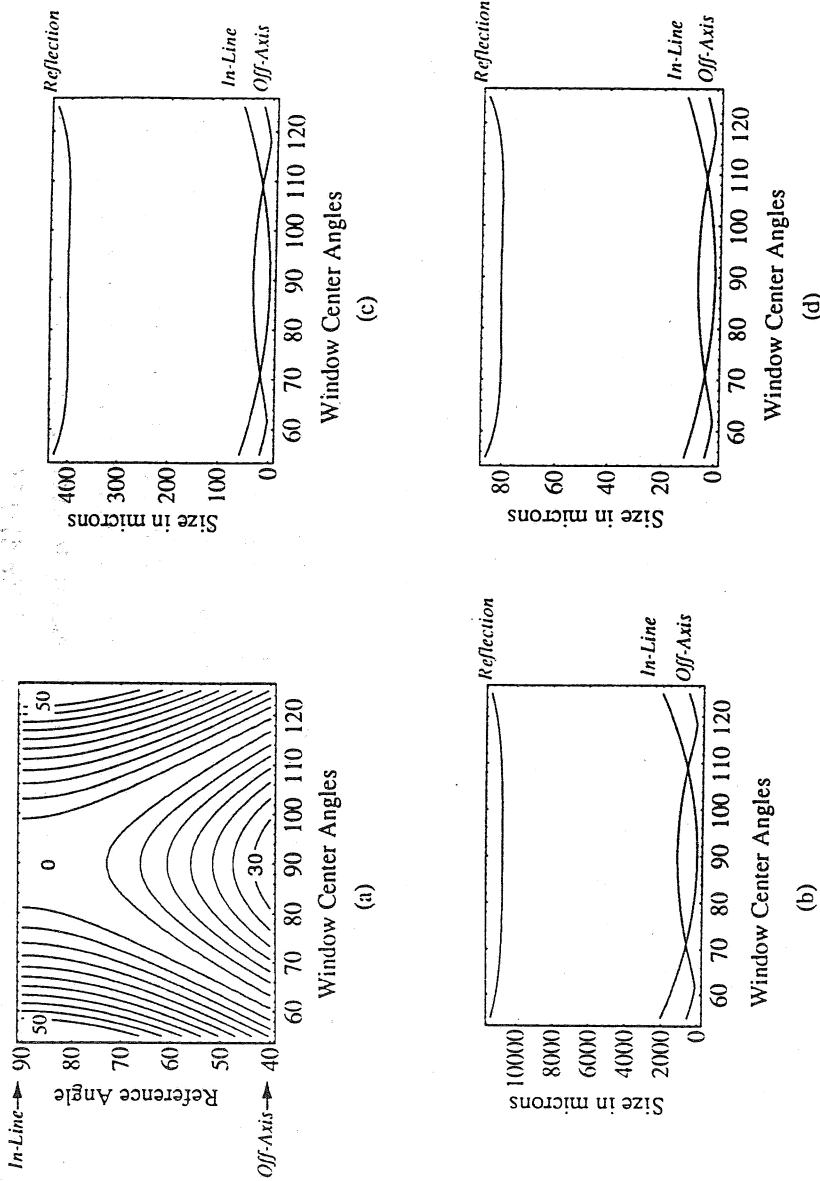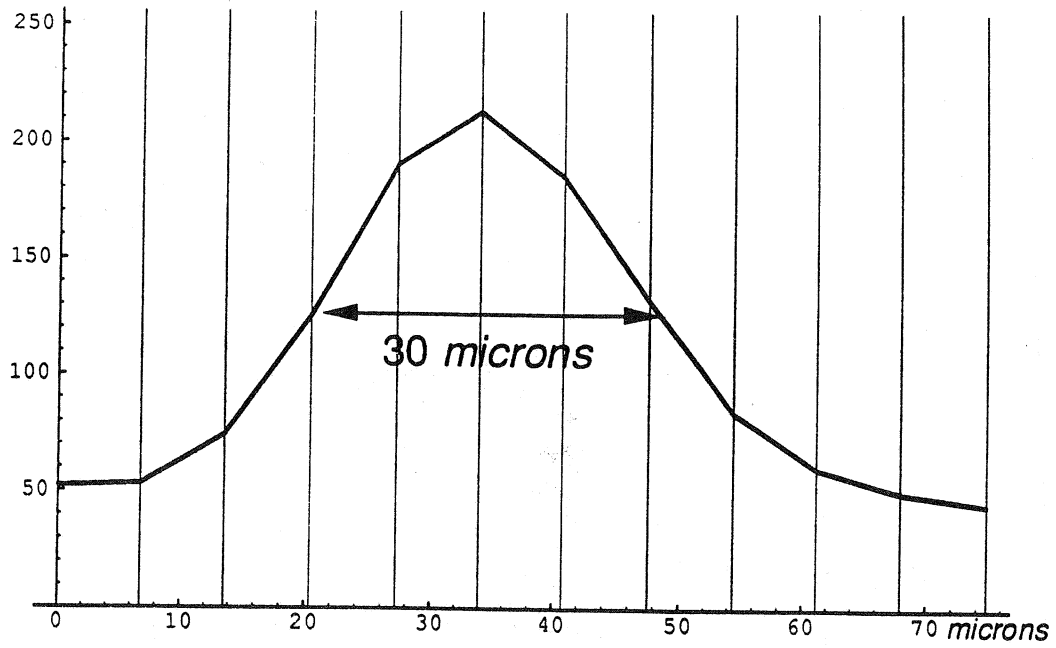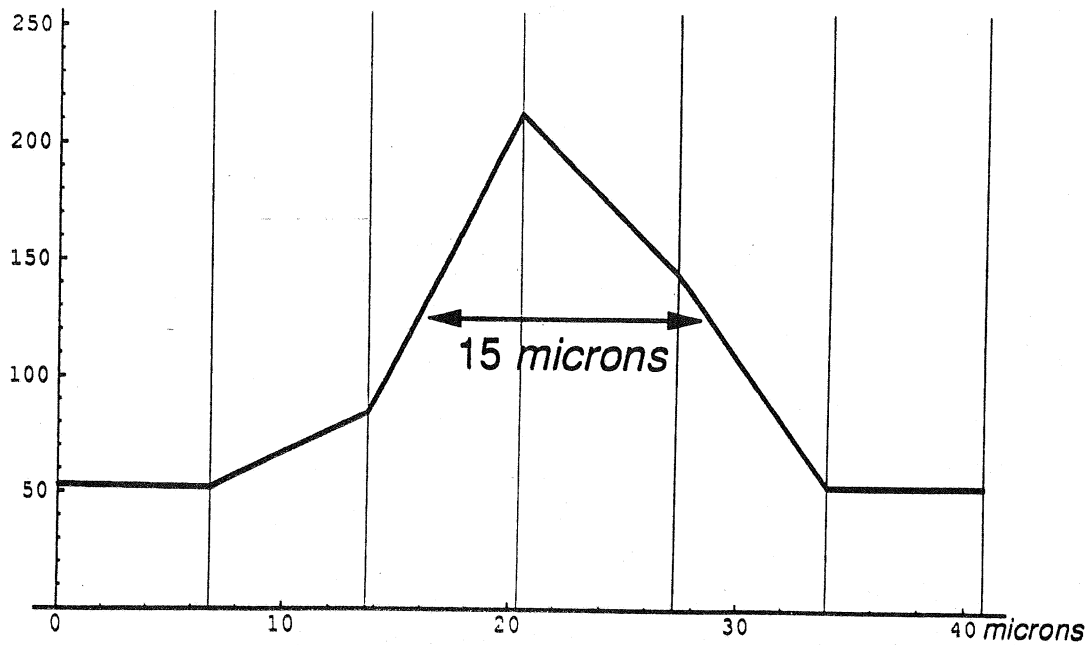
Figure 5

a) Contour plot of the wave vector displacement range $d_s (\theta_{max} - \theta_{min}) |_{window}$ as a function of the center window angle and reference beam angle for a 10° window, a 0.5% emulsion shrinkage, and an effective distance $d_s = 250$ *mm*. Contours have 5 *micron* intervals. Two of the recording geometries are labeled on the y-axis. The reflection geometry ($\theta_r = -40°$) is not shown. b)-d) Slices of the contour plot for fixed reference beam angles ($\theta_r = 90°, 40°, -40°$) corresponding to each geometry (in-line, off-axis, reflection) for different values of S b) 15% c) 0.5% d) 0.1%. Note that the off-axis geometry produces smaller displacement sizes over the *entire* range of angles that are imaged by the system.

Figure 6

A single reconstructed particle image. a) Horizontal scan showing a 30 *micron* particle image size. b) Vertical scan showing a 15 *micron* particle image size. The larger horizontal image size is due to the recorded grating vectors being horizontal.
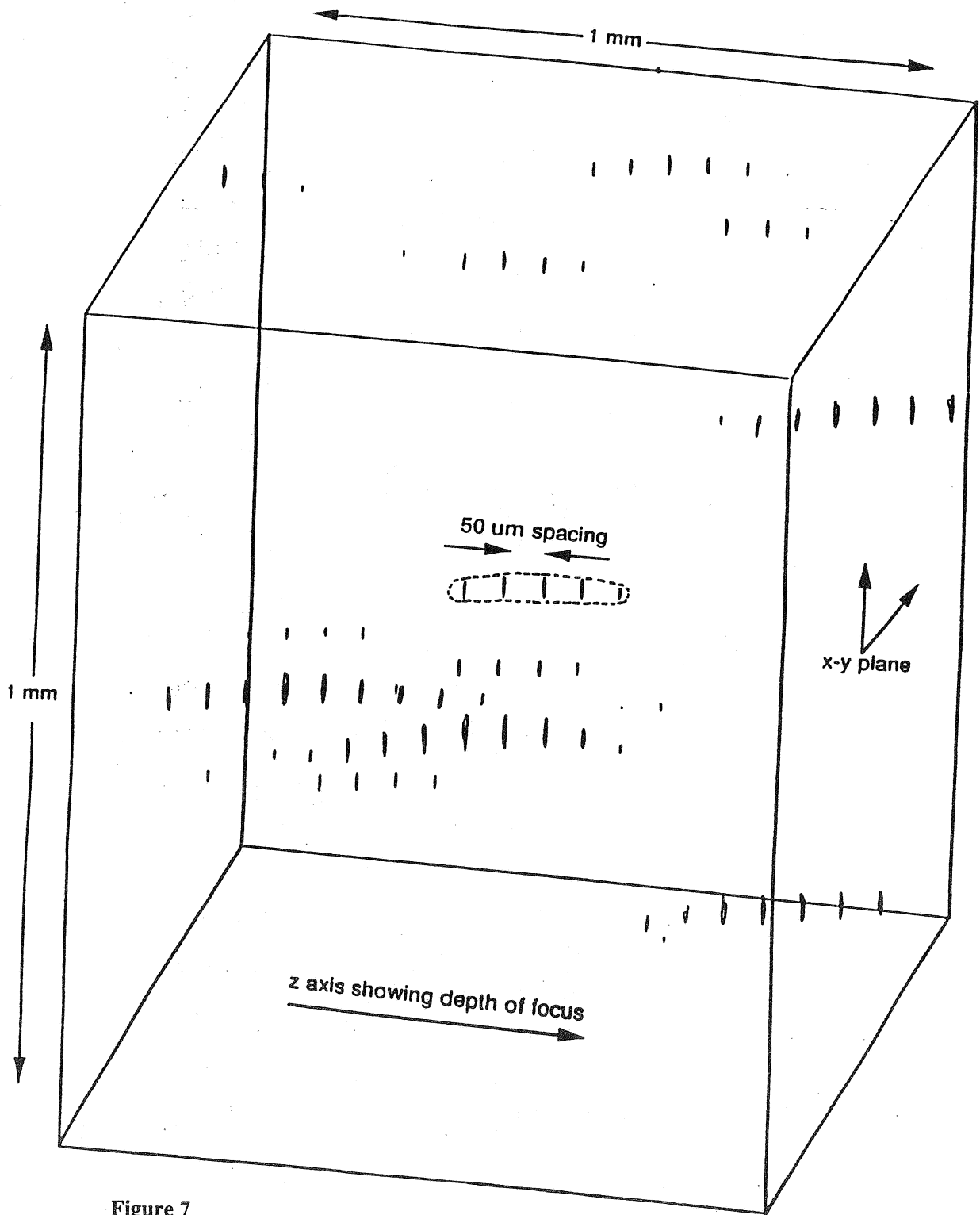

(a)

(b)

Figure 7

The *sampled* three-dimensional particle images are shown within a 1 mm^3 volume cell, imaged from a single reconstruction channel. Each stack of image slices forms an elongated ellipsoid structure, whose length ranges between 100 and 700 *microns* and provides a measure of depth-of-focus. The original particles were 0.5-1 *micron* in size.

Figure 8

Schematic of the two images at times *t1* and *t2* within the image volume for a single imaging channel. For clarity, the phase-conjugate recording and reconstruction through L_{11}-P_1-L_{12} is depicted as a single lens projection system **L** having unity magnification. The displacement along the CCD array is d**X** and the actual displacement of the particle is d**x**=**u***dt*.
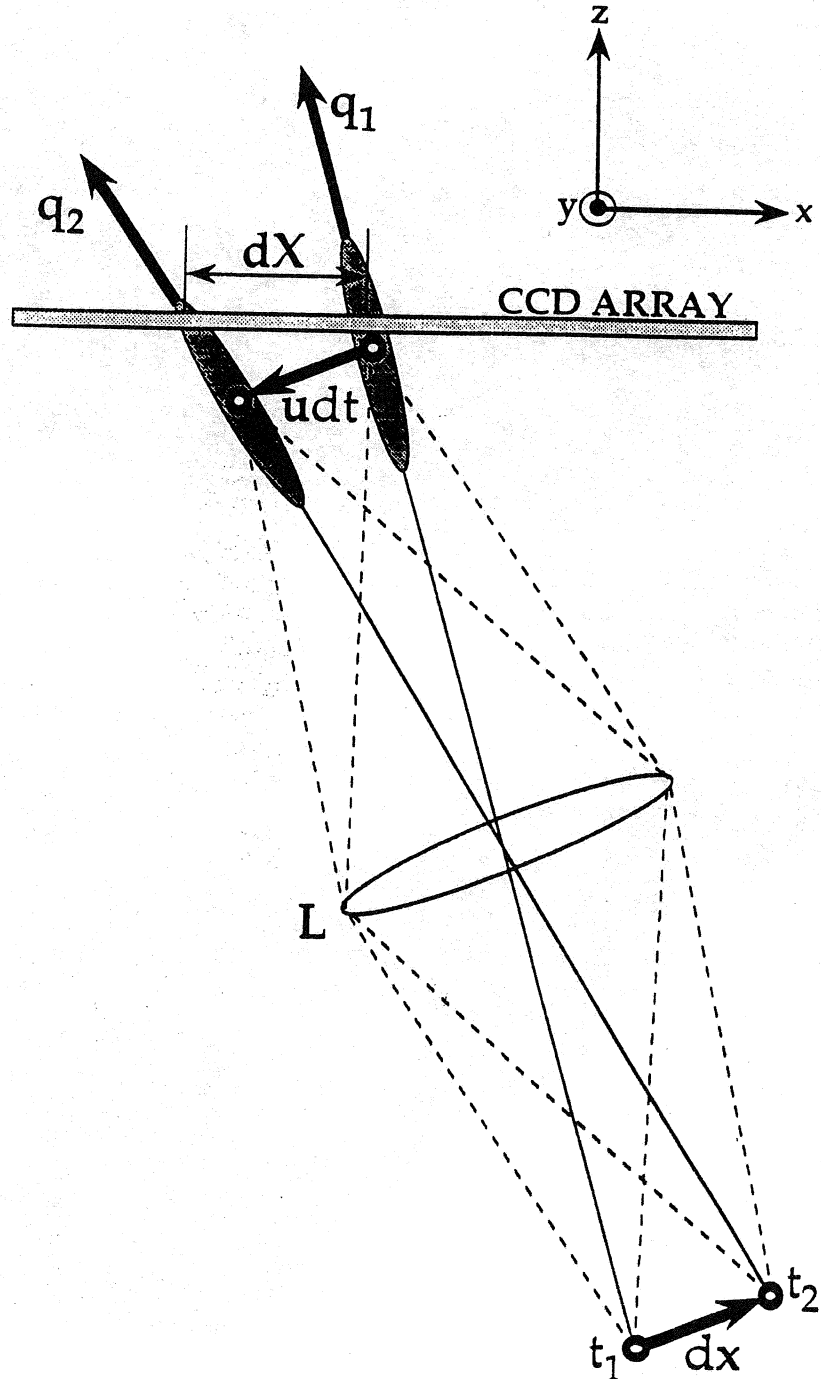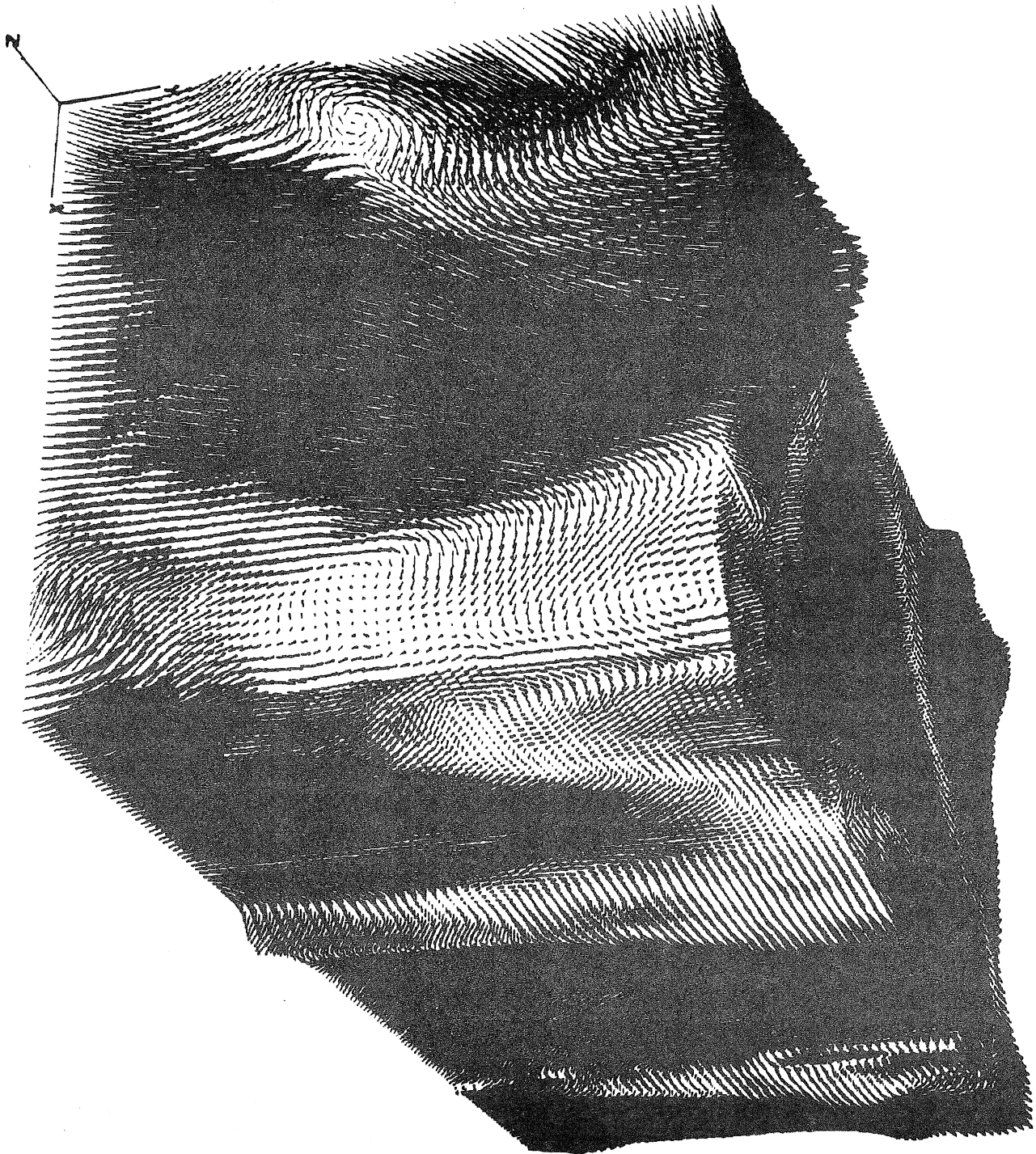
Figure 9

Complete 3-D vector field volume, from a pipe channel flow, showing the measured vectors along the sides of the $24.5 \times 24.5 \times 60 \ mm^3$ measurement volume, based on cross-correlation of the particle images. More than 400,000 3-D velocity vectors have been extracted from the measurement volume. Vectors have their mean velocity subtracted (0.8 m/s).

List of Recent TAM Reports

No.	Authors	Title	Date
705	Stewart, D. S., and J. B. Bdzil	Asymptotics and multi-scale simulation in a numerical combustion laboratory	Jan. 1993
706	Hsia, K. J., Y.-B. Xin, and L. Lin	Numerical simulation of semi-crystalline nylon 6: Elastic constants of crystalline and amorphous parts	Jan. 1993
707	Hsia, K. J., and J. Q. Huang	Curvature effects on compressive failure strength of long fiber composite laminates	Jan. 1993
708	Jog, C. S., R. B. Haber, and M. P. Bendsøe	Topology design with optimized, self-adaptive materials	Mar. 1993
709	Barkey, M. E., D. F. Socie, and K. J. Hsia	A yield surface approach to the estimation of notch strains for proportional and nonproportional cyclic loading	Apr. 1993
710	Feldsien, T. M., A. D. Friend, G. S. Gehner, T. D. McCoy, K. V. Remmert, D. L. Riedl, P. L. Scheiberle, and J. W. Wu	Thirtieth student symposium on engineering mechanics, J. W. Phillips, coord.	Apr. 1993
711	Weaver, R. L.	Anderson localization in the time domain: Numerical studies of waves in two-dimensional disordered media	Apr. 1993
712	Cherukuri, H. P., and T. G. Shawki	An energy-based localization theory: Part I—Basic framework	Apr. 1993
713	Manring, N. D., and R. E. Johnson	Modeling a variable-displacement pump	June 1993
714	Birnbaum, H. K., and P. Sofronis	Hydrogen-enhanced localized plasticity—A mechanism for hydrogen-related fracture	July 1993
715	Balachandar, S., and M. R. Malik	Inviscid instability of streamwise corner flow	July 1993
716	Sofronis, P.	Linearized hydrogen elasticity	July 1993
717	Nitzsche, V. R., and K. J. Hsia	Modelling of dislocation mobility controlled brittle-to-ductile transition	July 1993
718	Hsia, K. J., and A. S. Argon	Experimental study of the mechanisms of brittle-to-ductile transition of cleavage fracture in silicon single crystals	July 1993
719	Cherukuri, H. P., and T. G. Shawki	An energy-based localization theory: Part II—Effects of the diffusion, inertia and dissipation numbers	Aug. 1993
720	Aref, H., and S. W. Jones	Chaotic motion of a solid through ideal fluid	Aug. 1993
721	Stewart, D. S.	Lectures on detonation physics: Introduction to the theory of detonation shock dynamics	Aug. 1993
722	Lawrence, C. J., and R. Mei	Long-time behavior of the drag on a body in impulsive motion	Sept. 1993
723	Mei, R., J. F. Klausner, and C. J. Lawrence	A note on the history force on a spherical bubble at finite Reynolds number	Sept. 1993
724	Qi, Q., R. E. Johnson, and J. G. Harris	A re-examination of the boundary layer attenuation and acoustic streaming accompanying plane wave propagation in a circular tube	Sept. 1993
725	Turner, J. A., and R. L. Weaver	Radiative transfer of ultrasound	Sept. 1993
726	Yogeswaren, E. K., and J. G. Harris	A model of a confocal ultrasonic inspection system for interfaces	Sept. 1993
727	Yao, J., and D. S. Stewart	On the normal detonation shock velocity–curvature relationship for materials with large activation energy	Sept. 1993
728	Qi, Q.	Attenuated leaky Rayleigh waves	Oct. 1993
729	Sofronis, P., and H. K. Birnbaum	Mechanics of hydrogen–dislocation–impurity interactions: Part I—Increasing shear modulus	Oct. 1993
730	Hsia, K. J., Z. Suo, and W. Yang	Cleavage due to dislocation confinement in layered materials	Oct. 1993
731	Acharya, A., and T. G. Shawki	A second-deformation-gradient theory of plasticity	Oct. 1993
732	Michaleris, P., D. A. Tortorelli, and C. A. Vidal	Tangent operators and design sensitivity formulations for transient nonlinear coupled problems with applications to elasto-plasticity	Nov. 1993
733	Michaleris, P., D. A. Tortorelli, and C. A. Vidal	Analysis and optimization of weakly coupled thermo-elasto-plastic systems with applications to weldment design	Nov. 1993

(continued)

List of Recent TAM Reports (cont'd)

No.	Authors	Title	Date
734	Ford, D. K., and D. S. Stewart	Probabilistic modeling of propellant beds exposed to strong stimulus	Nov. 1993
735	Mei, R., R. J. Adrian, and T. J. Hanratty	Particle dispersion in isotropic turbulence under the influence of non-Stokesian drag and gravitational settling	Nov. 1993
736	Dey, N., D. F. Socie, and K. J. Hsia	Static and cyclic fatigue failure at high temperature in ceramics containing grain boundary viscous phase: Part I—Experiments	Nov. 1993
737	Dey, N., D. F. Socie, and K. J. Hsia	Static and cyclic fatigue failure at high temperature in ceramics containing grain boundary viscous phase: Part II—Modelling	Nov. 1993
738	Turner, J. A., and R. L. Weaver	Radiative transfer and multiple scattering of diffuse ultrasound in polycrystalline media	Nov. 1993
739	Qi, Q., and R. E. Johnson	Resin flows through a porous fiber collection in pultrusion processing	Dec. 1993
740	Weaver, R. L., W. Sachse, and K. Y. Kim	Transient elastic waves in a transversely isotropic plate	Dec. 1993
741	Zhang, Y., and R. L. Weaver	Scattering from a thin random fluid layer	Dec. 1993
742	Weaver, R. L., and W. Sachse	Diffusion of ultrasound in a glass bead slurry	Dec. 1993
743	Sundermeyer, J. N., and R. L. Weaver	On crack identification and characterization in a beam by nonlinear vibration analysis	Dec. 1993
744	Li, L., and N. R. Sottos	Predictions of static displacements in 1–3 piezocomposites	Dec. 1993
745	Jones, S. W.	Chaotic advection and dispersion	Jan. 1994
746	Stewart, D. S., and J. Yao	Critical detonation shock curvature and failure dynamics: Developments in the theory of detonation shock dynamics	Feb. 1994
747	Mei, R., and R. J. Adrian	Effect of Reynolds-number-dependent turbulence structure on the dispersion of fluid and particles	Feb. 1994
748	Liu, Z.-C., R. J. Adrian, and T. J. Hanratty	Reynolds-number similarity of orthogonal decomposition of the outer layer of turbulent wall flow	Feb. 1994
749	Barnhart, D. H., R. J. Adrian, and G. C. Papen	Phase-conjugate holographic system for high-resolution particle image velocimetry	Feb. 1994